

Low-velocity impact response of laminated FG-CNT reinforced composite plates in thermal environment

Farzad Ebrahimi* and Sajjad Habibi

*Department of Mechanical Engineering, Faculty of Engineering,
Imam Khomeini International University, Qazvin, Iran*

(Received November 26, 2016, Revised January 29, 2017, Accepted February 05, 2017)

Abstract. In this study, nonlinear response of laminated functionally graded carbon nanotube reinforced composite (FG-CNTRC) plate under low-velocity impact based on the Eshelby-Mori-Tanaka approach in thermal conditions is studied. The governing equations are derived based on higher-order shear deformation plate theory (HSDT) under von Kármán geometrical nonlinearity assumptions. The finite element method with 15 DOF at each node and Newmark's numerical integration method is applied to solve the governing equations. Four types of distributions of the uniaxially aligned reinforcement material through the thickness of the plates are considered. Material properties of the CNT and matrix are assumed to be temperature dependent. Contact force between the impactor and the laminated plate is obtained with the aid of the modified nonlinear Hertzian contact law models. In the numerical example, the effect of layup (stacking sequence) and lamination angle as well as the effect of temperature variations, distribution of CNTs, volume fraction of the CNTs, the mass and the velocity of the impactor in a constant energy level and boundary conditions on the impact response of the CNTRC laminated plates are investigated in details.

Keywords: nonlinear low-velocity impact; carbon nanotube; laminated FG-CNTRC; thermal environment; Eshelby-Mori-Tanaka

1. Introduction

Carbon nanotubes (CNTs) have exceptional electrical and thermal properties as well as extraordinary stiffness, strength, and corrosion resistance. For improvement of the multi functionality of fiber-reinforced composites, CNTs are an ideal candidate as nanoscale reinforcement. Their tensile strength of over 150 GPa and elastic modulus of over 1 TPa make them much stronger and stiffer than steel while being three to five times lighter (Kim *et al.* 2009). Research groups have demonstrate that mechanical properties of composites can strongly increase by adding a few weight percent (wt.%) of CNTs (Spitalsky *et al.* 2010, Sahoo *et al.* 2010). Due to high strength and stiffness to weight ratio and other improved mechanical properties of the CNRC, the laminated plates composed of these advanced composite materials have been employed as structural members in modern industries such as military, aerospace and marine. Up to now, several size-dependent theories are suggested for the analysis of nanostructures (Ebrahimi and Barati 2016a-e). Ebrahimi and Barati (2016f-i) proposed a nonlocal third-order shear deformable

*Corresponding author, Ph.D., E-mail: febrahimi@eng.ikiu.ac.ir

beam model for vibration and buckling analysis of nanobeams and nanoplates under various physical fields. They also (Ebrahimi and Barati 2016g-l) explored thermal and hygro-thermal effects on nonlocal behavior of nonhomogeneous nanoscale beams. Also Ebrahimi and Barati (2016m-r) examined buckling of functionally graded piezomagnetic nanoplates based on nonlocal elasticity. Furthermore distribution of CNTs in a polymeric matrix may be uniform or functionally graded (FG) (Liew *et al.* 2015) However, the previous studies demonstrate that uniform distribution of CNTs as the reinforcements in the composite can only attain moderate improvement of the mechanical properties (Qian *et al.* 2000, Seidel and Lagoudas 2006). Shen introduced the idea of using functionally graded carbon nanotube reinforced composite (Shen 2009). He showed that by using the graded distribution through the matrix of CNTs, the bending behavior of CNTs reinforced composites can be substantially enhanced.

Although studies of properties of carbon nanotube reinforced composites are quite beneficial, the ultimate aim of development of this advanced material is to explore potential applications of CNTRCs in actual structures. The static and dynamic analysis of CNTRC layers and laminates investigated by some researchers in recent years, which are briefly reviewed.

Formica *et al.* (2010) studied vibration behaviors of CNT-reinforced composite plates using the finite element method. The material properties of CNTRCs estimated through an equivalent continuum model based on the Eshelby-Mori-Tanaka approach. The nonlinear free vibration of CNT/fiber/polymer multi-scale composite plates with surface-bonded piezoelectric actuators is investigated by Rafiee *et al.* (2014). A perturbation scheme of multiple time scales is employed to determine the nonlinear vibration response. Yas and Heshmati (2012) using the finite element method, presented dynamic analysis of CNTRC beam under the action of moving load. Eshelby–Mori–Tanaka approach based on an equivalent fiber employed to estimate material properties of the beam. Zhu *et al.* (2012) analyzed free vibration and bending behaviors of FG-CNTRC plates by employing the rule of mixture. They used the FEM to solve the problem. Aragh *et al.* (2012) using the 2-D generalized differential quadrature method (GDQM), studied vibrational behavior of continuously graded CNT–reinforced cylindrical panels. An equivalent continuum model based on the Eshelby–Mori–Tanaka approach is employed to estimate the effective properties of CNTRCs. Lei *et al.* (2013) investigated the buckling analysis of FG-CNTRC plates under various in-plane mechanical loads based on either the extended rule of mixture or the Eshelby-Mori-Tanaka approach. They used the element-free kp-Ritz method to solve the problem. Alibeigloo and Liew (2013) studied the bending behavior of FG-CNTRC plate under thermo-mechanical loads based on three-dimensional theory of elasticity. Malekzadeh and Zarei (2014) investigated the free vibration behavior of quadrilateral laminated plates with CNTRC layers. Arani *et al.* (2011) presented buckling analysis of laminated CNT reinforced composite plates using FEM and analytical method. Based on the first-order shear deformation theory FSDT of plates, Malekzadeh and Shojaee (2013) studied the buckling behavior of quadrilateral laminated plates consisting of CNTRC layers. The stability equations are obtained using the adjacent equilibrium (Treffitz) buckling criterion. Heydarpour *et al.* (2014) studied the effect of Coriolis and centrifugal forces on the free vibration behavior of CNT reinforced composite truncated conical shells. Based on the first-order shear deformation shell theory, Jooybar *et al.* (2016) investigated the vibration behavior of FG-CNTRC truncated conical panels in thermal environment. They used the differential quadrature method (DQM) to solve the problem. Wang and Shen (2011) examined the large amplitude vibration of CNT reinforced composites on elastic foundation under thermal conditions. In another work, they studied the nonlinear bending and the large amplitude vibration of a sandwich plate with CNTRC face sheets on elastic foundation under thermal conditions (Wang and Shen 2012b). Also, they

presented the nonlinear dynamic response of single layered CNTRC plates resting on elastic foundations under thermal conditions (Wang and Shen 2012a). Shen and Zhang (2012a, b) studied the large amplitude vibration, non-linear bending and postbuckling behaviors of FG-CNTRC laminated plates resting on Pasternak elastic foundations under different hygrothermal environments conditions. In all of these interesting works, the governing differential equations were obtained using the HSDT plate theory, which were solved for simply supported plates using a two-step perturbation technique. Based on the FSDT plate theory, Lei *et al.* (2015) presented free vibration analyses of laminated FG-CNT reinforced composite plates using the kp-Ritz method. Based on the higher-order shear deformation beam theory, Shen *et al.* (2017) analyzed the free vibration behavior of the pre-twisted FG-CNTRC beams in thermal environment.

On the other hand, Rafiee and Moghadam (2012) simulated the impact and post-impact behavior of nanotube-reinforced polymer based on multi-scale finite element model software. Malekzadeh and Dehbozorgi (2016) studied response of FG-CNTRC skew plates plate under low-velocity impact based on the FSDT plate theory. The material properties of nanocomposite plates are estimated using Mori-Tanaka micro-mechanical model. Jam and Kiani (2015) presented the response of FG-CNTRC beams under low velocity impact based on the first order beam theory. Properties of the nanocomposite are estimated by applying a refined rule of mixture approach. Wang *et al.* (2014) analyzed the nonlinear low velocity impact response of temperature-dependent nanotube-reinforced composite plates under thermal by applying the rule of mixture. They used the perturbation technique to solve the problem for simply supported plates.

In the present work, response of laminated FG-CNTRCs plates under nonlinear low-velocity impact based on the Eshelby–Mori–Tanaka approach in thermal conditions is performed. The governing equations are derived based on higher-order shear deformation plate theory (HSDT) and von Kármán geometrical nonlinearity. The C^1 continuity finite element method with 15 DOF at each node and Newmark's numerical integration method is applied to solve the governing equations. The boundary conditions of plate are assumed to be clamped and simply supported.

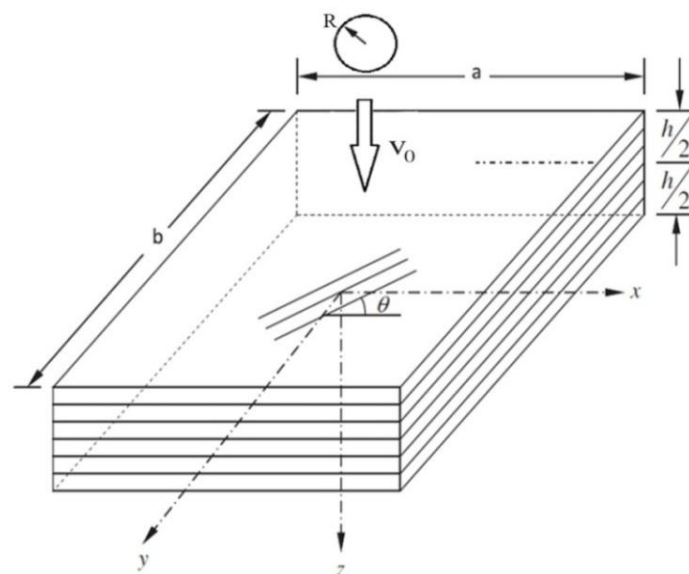


Fig. 1 The geometry of the laminated FG-CNTRCs plates

Four types of distributions of the uniaxially aligned reinforcement material through the thickness of the plates are considered. Material properties of the CNT and matrix are assumed to be temperature dependent. Contact force between the impactor and the laminated plate is obtained with the aid of the modified nonlinear Hertzian contact law models. In the numerical example, the effect of layup (stacking sequence) and lamination angle as well as the effect of temperature variations, distribution of CNTs, volume fraction of the CNTs, the mass and the velocity of the impactor in a constant energy level and boundary conditions on the impact response of the CNTRC laminated plates are investigated in details.

2. Theoretical formulation

2.1 Carbon nanotube reinforced composite plates

Consider rectangular laminated composite plates composed of perfectly bonded FG-CNT reinforced composite impacted by a low-velocity spherical impactor whose radius and initial velocity are illustrated by R and V_0 , respectively (Fig. 1). The coordinate system and geometric parameters used for the plate are depicted in Fig. 1. The CNTs are assumed to be functionally graded along the thickness direction of the layers and to be uniaxially aligned in axial direction. Based on distributions of CNTs (Fig. 2), CNT volume fractions $V_{CNT}(z)$ are given by

$$V_{CNT}(z) = \begin{cases} V_{CNT}^*(UD) \\ \left(1 - \frac{2z}{h}\right) V_{CNT}^* & (FG - \Lambda) \\ 2 \left(1 - \frac{2|z|}{h}\right) V_{CNT}^* & (FG - O) \\ 2 \left(\frac{2|z|}{h}\right) V_{CNT}^* & (FG - X) \end{cases} \quad (1)$$

where

$$V_{CNT}^* = \frac{w_{CNT}}{w_{CNT} + \left(\frac{\rho^{CNT}}{\rho^m}\right) - \left(\frac{\rho^{CNT}}{\rho^m}\right) w_{CNT}} \quad (2)$$

where w_{CNT} is the fraction of mass of the carbon nanotubes, and ρ^m and ρ^{CNT} are densities of the matrix and carbon nanotube, respectively. Note that the other three types FG-CNTRC plates and UD-CNTRC plate have the same overall mass fraction (w_{CNT}) of volume of CNTs.

Research groups have demonstrate that the material properties of CNT-reinforced materials are very dependent on the structure of CNTs (Li *et al.* 2007, Esawi and Farag 2007); effective material properties of the CNTRC are obtained through a several of micromechanics techniques, such as Eshelby-Mori-Tanaka approach (Wang and Pyrz 2004, Aragh *et al.* 2012) and the rule of mixture (Shen 2011, Shen and Zhang 2010). The Eshelby-Mori-Tanaka approach, based on the equivalent elastic inclusion idea of Eshelby and the concept of average stress in the matrix due to Mori and Tanaka, is also known as the equivalent inclusion-average stress method. In the light of Benveniste's revision (Benveniste 1987), effective elastic module tensor \mathbf{L} of the plates can be expressed as

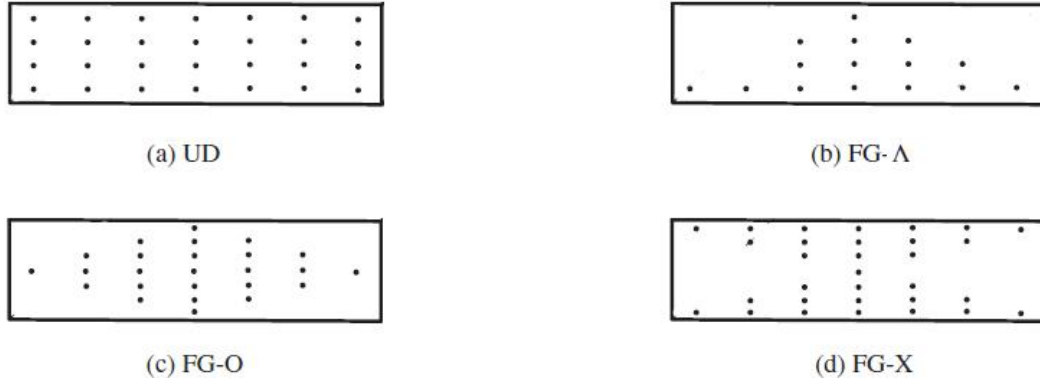


Fig. 2 Different types of CNTs distributions through the CNTRC layer. (a) UD layer; (b) FG- Λ layer; (c) FG-O panel; (d) FG-X panel

$$\mathbf{L} = \mathbf{L}_m + V_{CNT} \langle (\mathbf{L}_{CNT} - \mathbf{L}_m) \cdot \mathbf{A} \rangle \cdot [V_m \mathbf{I} + V_{CNT} \langle \mathbf{A} \rangle]^{-1} \quad (3)$$

where \mathbf{L}_{CNT} is stiffness tensors of CNT, \mathbf{L}_m is the stiffness tensor of the polymer matrix, and \mathbf{I} is the fourth-order unit tensor. The angular bracket indicates the average over all orientations. \mathbf{A} is the dilute mechanical strain concentration tensor and is given as

$$\mathbf{A} = [\mathbf{I} + \mathbf{S} \cdot \mathbf{L}_m^{-1} \cdot (\mathbf{L}_{CNT} - \mathbf{L}_m)]^{-1} \quad (4)$$

where \mathbf{S} is the Eshelby tensor (Eshelby 1957). The elements of \mathbf{S} are functions of the aspect ratio of the inclusion, s , and the Poisson's ratio of the matrix. The Mentioned relations were applied to obtain the elastic constants of nanocomposites as a function of CNT dispersion, volume fraction and aspect ratio. Table1 lists the elements of the Eshelby tensor for Ellipsoid and circular cylindrical inclusions. The variables in the Table 1 are given by

$$I_1 = \frac{2s}{\sqrt{(1-s^2)^3}} \left[s\sqrt{(s^2-1)} - \cosh^{-1}(s) \right]; \quad Q = \frac{3}{8(1-\nu^m)}, \quad R = \frac{1-2\nu^m}{8(1-\nu^m)} \quad (5)$$

$$T = Q \frac{4-3I_1}{3(s^2-1)}, \quad I_3 = 4-3I_1$$

As a check on the numerical analysis, it was verified that the results for very large aspect ratios ($s = 10^4$) converge with the results obtained by using the Eshelby tensor for cylindrical inclusions (obtained in the limit $s \rightarrow \infty$). The longitudinal and transverse coefficients of thermal expansion, α_{11} and α_{22} , respectively. Poisson's ratio ν_{12} and the mass densities ρ of the CNTRC plates is given as (Wang *et al.* 2014)

$$\nu_{12} = V_{CNT} \nu_{12}^{CNT} + V_m \nu^m \quad (6)$$

$$\rho = V_{CNT} \rho^{CNT} + V_m \rho^m \quad (7)$$

$$\alpha_{11} = \frac{V_{CNT} E_{11}^{CNT} \alpha_{11}^{CNT} + V_m E^m \alpha^m}{V_{CNT} E_{11}^{CNT} + V_m E^m} \quad (8)$$

Table 1 The elements of the Eshelby tensor for Ellipsoid and circular cylindrical inclusions (Mura 2013)

	Ellipsoid (aspect ratio, s)	Circular cylinder (lim $s \rightarrow \infty$)
SS_{11}	$\frac{4Q}{3} + RI_3 + 2s^2T$	0
$SS_{22} = SS_{33}$	$Q + RI_1 + \frac{3T}{4}$	$\frac{5 - 4\nu^m}{8(1 - \nu^m)}$
$SS_{23} = SS_{32}$	$\frac{Q}{3} - RI_1 + \frac{4T}{3}$	$\frac{-1 + 4\nu^m}{8(1 - \nu^m)}$
$SS_{21} = SS_{31}$	$-RI_1 - s^2T$	$\frac{\nu^M}{2(1 - \nu^m)}$
$SS_{12} = SS_{13}$	$-RI_3 - T$	0
SS_{44}	$\frac{Q}{3} + RI_1 + \frac{T}{4}$	$\frac{3 - 4\nu^m}{8(1 - \nu^m)}$
$SS_{55} = SS_{66}$	$2R - \frac{RI_1}{2} - \frac{1 + s^2}{2}T$	$\frac{1}{4}$
For other SS_{ij}	0	0

$$\alpha_{22} = (1 + \nu_{12}^{CNT})V_{CNT} \alpha_{22}^{CNT} + (1 + \nu^m)V_m \alpha^m - \nu_{12} \alpha_{11} \quad (9)$$

where ν_{12}^{CNT} and ν^m are Poisson's ratios, and α_{11}^{CNT} , α_{22}^{CNT} and α^m are the thermal expansion coefficients of the carbon nanotube and matrix, respectively. Note that ν_{12} is weakly depended on the position.

2.2 Impact dynamics and contact law

For low velocity impact on laminates the contact force F_c exerted by a spherical impactor can be related to the indentation α using the modified nonlinear Hertz contact law as follows (Sun and Chen 1985)

$$F_c = k_c \alpha^{3/2} \quad (10)$$

where k_c is the modified Hertz contact stiffness proposed by Sun and Chen as (Sun and Chen 1985)

$$k_c = \frac{4}{3} E^* R_i^{1/2} \quad (11)$$

with

$$\frac{1}{E^*} = \frac{1 - \nu_i^2}{E_i} + \frac{1}{E_{22}} \quad (12)$$

where R_i , ν_i and E_i are the radius, Poisson's ratio and Young's modulus of the impactor, respectively and E_{22} is the transverse modulus of the surface of the composite lamina.

During the unloading and subsequent reloading, the contact force F_c can be defined respectively (Yang and Sun 1982)

$$\begin{aligned} F_c &= F_m [(\alpha - \alpha_0)/(\alpha_m - \alpha_0)]^{5/2} \\ F_c &= F_m [(\alpha - \alpha_0)/(\alpha_m - \alpha_0)]^{3/2} \end{aligned} \quad (13)$$

where α_m and F_m are the local indentation and maximum contact force during the loading phase, respectively. The permanent indentation α_0 equals to zero when α_m remains below a critical indentation (Yang and Sun 1982).

2.3 Displacement field and strains of CNTRC laminated plates

Based on the higher order shear-deformation theory (Reddy 2004), the displacement field of laminated plate theory can be expressed as

$$u(x, y, z, t) = u_0(x, y, t) + z\phi_x - c_1 z^3 \left(\phi_x + \frac{\partial w_0}{\partial x} \right); \quad (14)$$

$$v(x, y, z, t) = v_0(x, y, t) + z\phi_y - c_1 z^3 \left(\phi_y + \frac{\partial w_0}{\partial y} \right); \quad (15)$$

$$w(x, y, z, t) = w_0(x, y, t) \quad (16)$$

where u_0 , v_0 , and w_0 are the displacements at the mid-plane of the reference plane of the plate and ϕ_x and ϕ_y define rotations about the y and x axes, respectively and $c_1 = 4/3h^2$. This shear theory (Reddy 2004) is based on the assumption that the transverse shear strain and hence shear stress vanish on the top and bottom surfaces of the plate and are nonzero elsewhere. Thus, a shear correction factor is not required.

The strain–displacement relations, based on von Kármán’s large deformation assumption are

$$\begin{Bmatrix} \varepsilon_{xx} \\ \varepsilon_{yy} \\ \gamma_{xy} \end{Bmatrix} = \varepsilon_0 + z\varepsilon_1 + z^3\varepsilon_3, \quad \begin{Bmatrix} \gamma_{yz} \\ \gamma_{xz} \end{Bmatrix} = \gamma_0 + z^2\gamma_2 \quad (17)$$

where

$$\begin{aligned} \varepsilon_0 &= \begin{Bmatrix} \frac{\partial u_0}{\partial x} + \frac{1}{2} \left(\frac{\partial w_0}{\partial x} \right)^2 \\ \frac{\partial v_0}{\partial y} + \frac{1}{2} \left(\frac{\partial w_0}{\partial y} \right)^2 \\ \frac{\partial u_0}{\partial y} + \frac{\partial v_0}{\partial x} + \frac{\partial w_0}{\partial x} \frac{\partial w_0}{\partial y} \end{Bmatrix}, & \varepsilon_1 &= \begin{Bmatrix} \frac{\partial \phi_x}{\partial x} \\ \frac{\partial \phi_y}{\partial y} \\ \frac{\partial \phi_x}{\partial y} + \frac{\partial \phi_y}{\partial x} \end{Bmatrix} \\ \varepsilon_3 &= -c_1 \begin{Bmatrix} \frac{\partial \phi_x}{\partial x} + \frac{\partial^2 w_0}{\partial x^2} \\ \frac{\partial \phi_y}{\partial y} + \frac{\partial^2 w_0}{\partial y^2} \\ \frac{\partial \phi_x}{\partial y} + \frac{\partial \phi_y}{\partial x} + 2 \frac{\partial^2 w_0}{\partial x \partial y} \end{Bmatrix}, & \gamma_0 &= \begin{Bmatrix} \frac{\partial w_0}{\partial x} + \phi_x \\ \frac{\partial w_0}{\partial y} + \phi_y \end{Bmatrix}, & \gamma_2 &= -c_2 \begin{Bmatrix} \frac{\partial w_0}{\partial x} + \phi_x \\ \frac{\partial w_0}{\partial y} + \phi_y \end{Bmatrix} \end{aligned} \quad (18)$$

In the above relations, ε_{xx} , ε_{yy} and γ_{xy} are in-plane strains and γ_{yz} and γ_{xz} define transverse shear strains and $c_2 = 3c_1$.

The governing equations may be generated by using principle of virtual work

$$\int_{-\frac{h}{2}}^{\frac{h}{2}} \int_0^b \int_0^a \{\delta \varepsilon\}^T \{\sigma\} dx dy dz + \int_{-\frac{h}{2}}^{\frac{h}{2}} \int_0^b \int_0^a \rho (\ddot{u} \delta u + \ddot{v} \delta v + \ddot{w} \delta w) dx dy dz - \int_0^b \int_0^a q \delta w dx dy - F_c \delta \alpha = 0 \quad (19)$$

2.4 Constitutive equations

The constitutive relation of the k th layer of the laminate in the material axes can be stated as (Shu and Sun 1994)

$$\begin{Bmatrix} \sigma_1 \\ \sigma_2 \\ \tau_{23} \\ \tau_{31} \\ \tau_{12} \end{Bmatrix} = \begin{bmatrix} Q_{11}(z, T) & Q_{12}(z, T) & 0 & 0 & 0 \\ Q_{12}(z, T) & Q_{22}(z, T) & 0 & 0 & 0 \\ 0 & 0 & Q_{44}(z, T) & 0 & 0 \\ 0 & 0 & 0 & Q_{55}(z, T) & 0 \\ 0 & 0 & 0 & 0 & Q_{66}(z, T) \end{bmatrix} \begin{pmatrix} \begin{Bmatrix} \varepsilon_1 \\ \varepsilon_2 \\ \gamma_{23} \\ \gamma_{31} \\ \gamma_{12} \end{Bmatrix} - \begin{Bmatrix} \alpha_{11}(z, T) \\ \alpha_{22}(z, T) \\ 0 \\ 0 \\ 0 \end{Bmatrix} \Delta T \end{pmatrix} \quad (20)$$

where

$$\begin{aligned} Q_{11}(z, T) &= \frac{E_{11}(z, T)}{1 - \nu_{12}\nu_{21}}, & Q_{66}(z, T) &= G_{12}(z, T) \\ Q_{22}(z, T) &= \frac{E_{22}(z, T)}{1 - \nu_{12}\nu_{21}}, & Q_{44}(z, T) &= G_{23}(z, T) \\ Q_{12}(z, T) &= \frac{\nu_{12}E_{22}(z, T)}{1 - \nu_{12}\nu_{21}}, & Q_{55}(z, T) &= G_{13}(z, T) \end{aligned} \quad (21)$$

where ΔT is the temperature change with respect to a reference state. These properties are assumed to be temperature-dependent and to be graded along the thickness direction layer.

If the fiber angle with the geometric x axis is denoted the relation (20) can be transferred to the geometric coordinates as

$$\begin{Bmatrix} \sigma_x \\ \sigma_y \\ \tau_{yz} \\ \tau_{xz} \\ \tau_{xy} \end{Bmatrix}_k = \begin{bmatrix} \bar{Q}_{11}(z, T) & \bar{Q}_{12}(z, T) & 0 & 0 & \bar{Q}_{16}(z, T) \\ \bar{Q}_{12}(z, T) & \bar{Q}_{22}(z, T) & 0 & 0 & \bar{Q}_{26}(z, T) \\ 0 & 0 & \bar{Q}_{44}(z, T) & \bar{Q}_{45}(z, T) & 0 \\ 0 & 0 & \bar{Q}_{45}(z, T) & \bar{Q}_{55}(z, T) & 0 \\ \bar{Q}_{16}(z, T) & \bar{Q}_{26}(z, T) & 0 & 0 & \bar{Q}_{66}(z, T) \end{bmatrix}_k \quad (22)$$

$$\left(\begin{matrix} \varepsilon_x \\ \varepsilon_y \\ \gamma_{yz} \\ \gamma_{xz} \\ \gamma_{xy} \end{matrix} \right) - \left(\begin{matrix} \alpha_x(z, T) \\ \alpha_y(z, T) \\ 0 \\ 0 \\ \alpha_{xy}(z, T) \end{matrix} \right) \Delta T \quad (22)$$

where

$$\begin{aligned} \bar{Q}_{11} &= Q_{11} \cos^4 \theta + 2(Q_{12} + 2Q_{66}) \sin^2 \theta \cos^2 \theta + Q_{22} \sin^4 \theta \\ \bar{Q}_{12} &= (Q_{11} + Q_{22} - 4Q_{66}) \sin^2 \theta \cos^2 \theta + Q_{12} (\sin^4 \theta + \cos^4 \theta) \\ \bar{Q}_{22} &= Q_{11} \sin^4 \theta + 2(Q_{12} + 2Q_{66}) \sin^2 \theta \cos^2 \theta + Q_{22} \cos^4 \theta \\ \bar{Q}_{16} &= (Q_{11} - Q_{12} - 2Q_{66}) \sin \theta \cos^3 \theta + (Q_{12} - Q_{22} + 2Q_{66}) \sin^3 \theta \cos \theta \\ \bar{Q}_{26} &= (Q_{11} - Q_{12} - 2Q_{66}) \sin^3 \theta \cos \theta + (Q_{12} - Q_{22} + 2Q_{66}) \sin \theta \cos^3 \theta \\ \bar{Q}_{66} &= (Q_{11} + Q_{22} - 2Q_{12} - 2Q_{66}) \sin^2 \theta \cos^2 \theta + Q_{66} (\sin^4 \theta + \cos^4 \theta) \\ \bar{Q}_{44} &= Q_{44} \cos^2 \theta + Q_{55} \sin^2 \theta \\ \bar{Q}_{45} &= (Q_{55} - Q_{44}) \cos \theta \sin \theta \\ \bar{Q}_{55} &= Q_{55} \cos^2 \theta + Q_{44} \sin^2 \theta \end{aligned} \quad (23a)$$

$$\begin{aligned} \alpha_x &= \alpha_{11} \cos^2 \theta + \alpha_{22} \sin^2 \theta \\ \alpha_y &= \alpha_{11} \sin^2 \theta + \alpha_{22} \cos^2 \theta \\ \alpha_{xy} &= 2\alpha_{11} \cos \theta \cdot \sin \theta - 2\alpha_{22} \cos \theta \cdot \sin \theta \end{aligned} \quad (23b)$$

3. FEM formulations for the CNRC laminated plates in thermal environments

In present section, the equations of CNRC laminated plates under thermal conciliations by using finite element method are discretized. Based on Eq. (19), one may write

$$\begin{aligned} &\left\{ \int_{-\frac{h}{2}}^{\frac{h}{2}} \int_{\Omega_0} \delta D_0^t (\iota_0 + z\iota_1 + z^3\iota_3 + \iota_N)^t Q_p \left(\iota_0 + z\iota_1 + z^3\iota_3 + \left(\frac{1}{2}\right)\iota_N \right) D_0 \right. \\ &+ \delta D_0^t (\iota_{s0} + z^2\iota_{s2})^t Q_s (\iota_{s0} + z^2\iota_{s2}) D_0 \\ &+ \delta D_0^t \rho (\iota_{\theta 0} + z\iota_{\theta 1} + z^3\iota_{\theta 3})^t (\iota_{\theta 0} + z\iota_{\theta 1} + z^3\iota_{\theta 3}) D_0 \left. \right\} d\Omega dz \\ &- \int_{\Omega_0} \delta D_0^t q^{Th} d\Omega - \delta D_0^t F_c = 0 \end{aligned} \quad (24)$$

where

$$Q_p = \begin{bmatrix} \bar{Q}_{11} & \bar{Q}_{12} & \bar{Q}_{16} \\ \bar{Q}_{12} & \bar{Q}_{22} & \bar{Q}_{26} \\ \bar{Q}_{16} & \bar{Q}_{26} & \bar{Q}_{66} \end{bmatrix}, \quad Q_s = \begin{bmatrix} \bar{Q}_{44} & \bar{Q}_{45} \\ \bar{Q}_{45} & \bar{Q}_{55} \end{bmatrix} \quad (25)$$

$$l_0 = \begin{bmatrix} \frac{\partial}{\partial x} & 0 & 0 & 0 & 0 \\ 0 & \frac{\partial}{\partial y} & 0 & 0 & 0 \\ \frac{\partial}{\partial y} & \frac{\partial}{\partial x} & 0 & 0 & 0 \end{bmatrix}, \quad l_1 = \begin{bmatrix} 0 & 0 & 0 & \frac{\partial}{\partial x} & 0 \\ 0 & 0 & 0 & 0 & \frac{\partial}{\partial y} \\ 0 & 0 & 0 & \frac{\partial}{\partial y} & \frac{\partial}{\partial x} \end{bmatrix}, \quad l_2 = 0 \quad (25)$$

$$l_3 = \frac{-4}{3h^2} \begin{bmatrix} 0 & 0 & \frac{\partial^2}{\partial x^2} & \frac{\partial}{\partial x} & 0 \\ 0 & 0 & \frac{\partial^2}{\partial y^2} & 0 & \frac{\partial}{\partial y} \\ 0 & 0 & 2\frac{\partial}{\partial y}\frac{\partial}{\partial x} & \frac{\partial}{\partial y} & \frac{\partial}{\partial x} \end{bmatrix}, \quad l_N = \begin{bmatrix} 0 & 0 & \frac{\partial w_0}{\partial x} \frac{\partial}{\partial x} & 0 & 0 \\ 0 & 0 & \frac{\partial w_0}{\partial y} \frac{\partial}{\partial y} & 0 & 0 \\ 0 & 0 & \frac{\partial w_0}{\partial x} \frac{\partial}{\partial y} + \frac{\partial w_0}{\partial y} \frac{\partial}{\partial x} & 0 & 0 \end{bmatrix}$$

$$l_{s0} = \begin{bmatrix} 0 & 0 & \frac{\partial}{\partial x} & 0 & 1 \\ 0 & 0 & \frac{\partial}{\partial y} & 1 & 0 \end{bmatrix}, \quad l_{s2} = \frac{-4}{h^2} \begin{bmatrix} 0 & 0 & \frac{\partial}{\partial x} & 0 & 1 \\ 0 & 0 & \frac{\partial}{\partial y} & 1 & 0 \end{bmatrix}, \quad l_{s1} = 0 \quad (26)$$

$$l_{\theta 0} = \begin{bmatrix} 1 & 0 & 0 & 0 & 0 \\ 0 & 1 & 0 & 0 & 0 \\ 0 & 0 & 1 & 0 & 0 \end{bmatrix}, \quad l_{\theta 1} = \begin{bmatrix} 0 & 0 & 0 & 1 & 0 \\ 0 & 0 & 0 & 0 & 1 \\ 1 & 0 & 0 & 0 & 0 \end{bmatrix},$$

$$l_{\theta 3} = -c_1 \begin{bmatrix} 0 & 0 & \frac{\partial}{\partial x} & 1 & 0 \\ 0 & 0 & \frac{\partial}{\partial y} & 0 & 1 \\ 0 & 0 & 0 & 0 & 0 \end{bmatrix}, \quad l_{\theta 2} = 0$$

and $\{D_0\}=\{u_0, v_0, w_0, \phi_x, \phi_y\}^t$ is the displacement vector of a point in middle-plane, and q^{Th} denote the thermal force and is given by

$$q^{Th} = (l_0 + z l_1 + z^3 l_3)^t Q_p \begin{Bmatrix} \alpha_x(z, T) \\ \alpha_y(z, T) \\ \alpha_{xy}(z, T) \end{Bmatrix} \Delta T \quad (27)$$

From the strain-displacement relationships, one can observe that the first and second-order derivatives of generalized displacements are appeared in equations. Therefore, to guarantee the integrability of equations, the C^1 -continuity of the generalized displacement functions is generally necessary in finite element procedure (Ebrahimi and Habibi 2016). Hence, in this paper, the four-noded rectangular conforming element based on HSDT is used. The element is C^1 -continuous via 15 DOF at each node.

According to the nodal displacement vector, the displacement vector of the reference plane may be written as

$$\mathbf{D}_0^{(e)} = \left(\begin{array}{ccc|ccc} \psi_1 & \dots & 0 & \psi_{4y} & \dots & 0 \\ 0 & & 0 & 0 & & 0 \\ 0 & \ddots & 0 & 0 & \ddots & 0 \\ 0 & & 0 & 0 & & 0 \\ 0 & \dots & \psi_1 & 0 & \dots & \psi_{4y} \end{array} \right)_{5 \times 60} \quad \{d^e\} = \boldsymbol{\psi} \mathbf{d}_0^{(e)} \quad (28)$$

where

$$\{d^e\} = \left\{ \begin{array}{l} u_{0i}, v_{0i}, w_{0i}, \phi_{xi}, \phi_{yi}, u_{0i,x}, v_{0i,x}, w_{i,x}, \\ \phi_{xi,x}, \phi_{yi,x}, u_{0i,y}, v_{0i,y}, w_{0i,y}, \phi_{xi,y}, \phi_{yi,y} \end{array} \right\}^T \text{ are the 15-DOF associated with each node.}$$

The displacement and rotation interpolation functions may be stated as

$$\psi_i = \frac{1}{8} (1 + \xi_i \xi) (1 + \eta_i \eta) (2 + \xi_i \xi + \eta_i \eta - \xi^2 - \eta^2), \quad (29)$$

$$\psi_{ix} = \frac{1}{8} \alpha \xi_i (1 + \xi_i \xi)^2 (1 + \eta_i \eta) (\xi_i \xi - 1), \quad (30)$$

$$\psi_{iy} = \frac{1}{8} b \eta_i (1 + \xi_i \xi) (\eta_i \eta - 1) (1 + \eta_i \eta)^2, \quad (31)$$

where α and β are the half length of element in the x and y directions and the normalized coordinates are

$$\xi = \frac{x - x_c}{\alpha}, \quad \eta = \frac{y - y_c}{\beta} \quad (32)$$

where (x_c, y_c) is the center of rectangular element. Based on Eqs. (28)-(32), Eq. (24) can be expressed as

$$\left. \left(\delta d^{(e)} \right)^t \left\{ \begin{array}{l} \int_{\Omega_0} \left[\sum_{i=0}^3 B_i^t (Q_i^{(e)} B_0 + Q_{i+1}^{(e)} B_1 + Q_{i+3}^{(e)} B_3) d^{(e)} \right. \right. \\ \quad + \\ \quad \left. \left. + \sum_{i=0}^2 B_{si}^t (B_{s0} + Q_{s(i+3)}^{(e)} B_{s2}) d^{(e)} \right. \right. \\ \quad \left. \left. + \sum_{i=0}^3 B_{\theta i}^t (I_i^{(e)} B_{\theta 0} + I_{i+1}^{(e)} B_{\theta 1} + I_{i+3}^{(e)} B_{\theta 3}) d^{(e)} - \right. \right. \\ \quad \left. \left. [B_0^t B_1^t \ B_3^t] \begin{bmatrix} q_0^{Th} \\ q_1^{Th} \\ q_3^{Th} \end{bmatrix} \right] \right\} d\Omega - \boldsymbol{\psi}^t F_c^{(e)} \right\} = 0 \quad (33)$$

where

$$q_i^{Th} = \int_{-h/2}^{h/2} \begin{bmatrix} \bar{Q}_{11} \alpha_{11} + \bar{Q}_{12} \alpha_{22} \\ \bar{Q}_{12} \alpha_{22} + \bar{Q}_{22} \alpha_{11} \\ \bar{Q}_{16} \alpha_{11} + \bar{Q}_{26} \alpha_{11} \end{bmatrix} z^i \Delta T dz \quad (34)$$

$$(B_0, B_1, B_3, B_N, B_{s0}, B_{s2}, B_{\theta 0}, B_{\theta 1}, B_{\theta 3}) = (t_0, t_1, t_3, t_N, t_{s0}, t_{s2}, t_{\theta 0}, t_{\theta 1}, t_{\theta 3})\psi$$

$$Q_i = \int_{-\frac{h}{2}}^{\frac{h}{2}} z^i Q dz, \quad Q_{si} = \int_{-\frac{h}{2}}^{\frac{h}{2}} z^i Q_s dz, \quad I_i = \int_{-\frac{h}{2}}^{\frac{h}{2}} z^i \rho dz, \quad i = 0, 1, 3 \quad (35)$$

Eq. (33) holds for any arbitrary $(\delta d^{(e)})^t \neq 0$, therefore in a compact form

$$K_L^{(e)} d_0^{(e)} + K_{NL}^{(e)} d_0^{(e)} + M^{(e)} \ddot{d}_0^{(e)} = F^{(e)} \quad (36)$$

where, the element stiffness matrixes $K_L^{(e)}, K_{NL}^{(e)}$, element mass matrix $M^{(e)}$, element load vector $F^{(e)}$, can be given as

$$K^{(e)} = K_L^{(e)} + K_{NL}^{(e)}$$

$$= \int_{\Omega_0} \left[\sum_{i=0}^3 B_i^t (Q_i^{(e)} B_0 + Q_{i+1}^{(e)} B_1 + Q_{i+3}^{(e)} B_3) + \sum_{i=0}^2 B_{si}^t (Q_{si}^{(e)} B_{s0} + Q_{s(i+3)}^{(e)} B_{s2}) \right] dx dy \quad (37)$$

$$+ B_N^t \left(Q_0^{(e)} B_0 + Q_1^{(e)} B_1 + Q_3^{(e)} B_3 + \left(\frac{1}{2}\right) Q_0^{(e)} B_N \right) + \left(\frac{1}{2}\right) (B_0 + B_1 + B_3) Q_0^{(e)} B_N$$

$$M^{(e)} = \int_{\Omega_0} \left[\sum_{i=0}^3 B_{\theta i}^t (I_i^{(e)} B_{\theta 0} + I_{i+1}^{(e)} B_{\theta 1} + I_{i+3}^{(e)} B_{\theta 3}) \right] dx dy \quad (38)$$

$$F^{(e)} = Y^{(e)} + \psi^t F_c^{(e)} \quad (39)$$

where $Y^{(e)}$ is the element force vector due to thermal and is given by

$$Y^{(e)} = \int_{\Omega_0^{(e)}} [B_0^t B_1^t B_3^t] \begin{bmatrix} q_0^{Th} \\ q_1^{Th} \\ q_3^{Th} \end{bmatrix} dx dy \quad (40)$$

Resulting time-dependent equations may be expressed as

$$[K]\{d\} + [M]\{\ddot{d}\} = \{F\} \quad (41)$$

where, d and \ddot{d} are respectively the displacement and acceleration vector. F is the global load vector, which includes the impact force and thermal force K is the global stiffness matrix, includes linear and nonlinear stiffness matrix. Also M denote the global mass matrix. The above global matrices and global load vectors can be obtained by assembling each corresponding element matrix and load vector, respectively.

The boundary conditions for clamped and simply supported conditions are given below

$$u_n = u_s = w_0 = \phi_n = \phi_s = 0 \quad (\text{Clamped edge})$$

$$u_s = w_0 = \phi_s = 0 \quad (\text{Simply supported edge})$$

where the subscripts n and s denote the normal and tangential directions, respectively, on the boundaries.

In order to solve Eq. (41), Newmark's numerical time integration method is used. Based on this method, accelerations and velocities of the end of each time step are computed by (Zienkiewicz and Taylor 2005)

$$\begin{aligned} \ddot{\Lambda}_{j+1} &= a_1(\Lambda_{j+1} - \Lambda_j) - a_2\dot{\Lambda}_j - a_3\ddot{\Lambda}_j \\ \dot{\Lambda}_{j+1} &= \dot{\Lambda}_j + a_4\ddot{\Lambda}_j + a_5\ddot{\Lambda}_j \end{aligned} \tag{42}$$

where j is the time step counter and

$$\begin{aligned} a_1 &= \frac{2}{\zeta(\Delta t)^2}; & a_2 &= \frac{2}{\zeta\Delta t}; & a_3 &= \frac{1}{\zeta} - 1; & \zeta &\leq \lambda \\ a_4 &= \Delta t(1 - \lambda); & a_5 &= \lambda\Delta t; & \lambda &\geq 0.5 \end{aligned} \tag{43}$$

By substituting Eq. (43) into Eq. (42), we obtain

$$\hat{K}_{j+1}\Lambda_{j+1} = \hat{F}_{j+1} \tag{44}$$

where

$$\hat{K}_{j+1} = K_{j+1} + a_1M_{j+1} \tag{45}$$

$$\hat{F}_{j+1} = H_jM_{j+1} + F_j \tag{46}$$

where H_j is the following vector

$$H_j = a_1\Lambda_i + a_2\dot{\Lambda}_i - a_3\ddot{\Lambda}_j \tag{47}$$

Since Eq. (41) is a nonlinear equation, Picard or Newton–Raphson method has to be employed in each time step to reach a convergence criterion, e.g.

$$\frac{\|\Lambda_i^{(\eta+1)} - \Lambda_i^{(\eta)}\|}{\Lambda_i^{(\eta+1)}} \cong \Delta \tag{48}$$

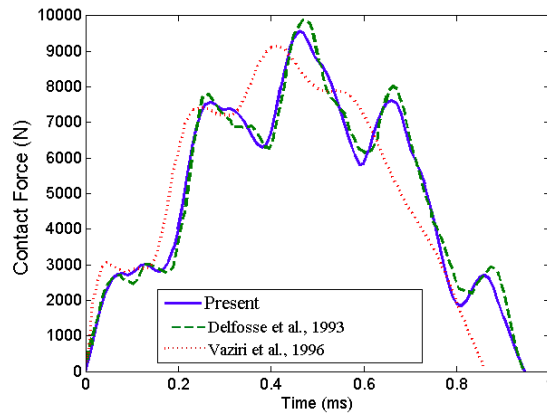


Fig. 3 Comparisons of contact force of an (CFRC) composite laminated plate

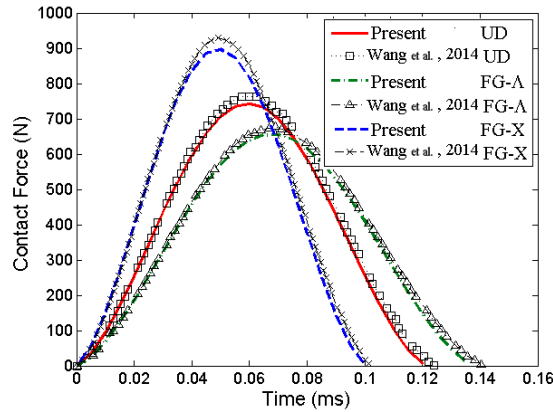


Fig. 4 Comparisons of contact force history of three types of CNTRC square plates

where i , η and Δ are the time step counter, iteration counter, and a sufficiently small number, respectively.

4. Results and discussions

In present section, after verification of the results, the effect of layup (stacking sequence) and lamination angle as well as the effect of temperature variations, distribution of CNTs, volume fraction of the CNTs, the mass and the velocity of the impactor in a constant energy level and boundary conditions on the impact response of the CNTRC laminated plates are investigated in details. Due to enable tracing time variations of the response more adequately, the time integration steps must be much less than the fundamental natural period of the structure. Hence in this paper, a time step that is equal or less than 10^{-6} (sec) is chosen. Also, $\Delta = 0.0001$ is used for the convergence criterion (Eq. (48)).

4.1 Validation

In order to validate the results of the present formulations two examples are considered. As a first example, response of carbon fiber reinforced (CFRC) composite laminated plates under low-velocity impact via a steel impactor is investigated. The geometrical and material parameters are set according to that in (Vaziri *et al.* 1996) and (Delfosse *et al.* 1993), of which the results are compared. Specifications of the impactor are $E_i = 207$ GPa, $\nu_i = 0.3$, $m_i = 0.314$ kg and the radius is 12.7 mm and initial velocity $V_0 = 7.7$ m/s; Material properties of the $[45/90/-45/0]_{3s}$ composite plate are $E_1 = 129$ GPa; $E_2 = 7.5$ GPa; $G_{12} = 3.5$ GPa; $\nu_{12} = 0.33$; $\rho = 1540$ kgm^{-3} . The plate is simply supported with dimensions of plate are $0.127 \times 0.0762 \times 0.00465$ (m). In Fig. 3 the results of this study for the contact force histories are compared with those FEM based presented results by (Vaziri *et al.* 1996) and those obtained experimentally by (Delfosse *et al.* 1993). As it is obvious from Fig. 3, results by the present approach are in good agreement with the experimental and the theoretical results in literature.

As a second example, contact force history of a simply supported the single-layer CNTRC is obtained from the present formulations and compared with the one investigated by (Wang *et al.*

Table 2 Material properties of the composite matrix (Zhang *et al.* 2014)

$$E^m = (3.52 - 0.0034T) \text{ GPa};$$

$$\alpha^m = 45(1 + 0.0005\Delta T) \times 10^{-6} \text{ 1/K}$$

$$\nu^m = 0.34; \quad \rho = 1150 \text{ Kg/m}^3$$

Table 3 Temperature-dependent material properties of (10, 10) SWCNT
($L = 9.26 \text{ nm}$, $R = 0.68 \text{ nm}$, $h = 0.067 \text{ nm}$, $\nu_{12}^{CNT} = 0.175$) (Wang *et al.* 2014)

Temperature (K)	E_{11}^{CNT} (TPa)	E_{22}^{CNT} (TPa)	G_{12}^{CNT} (TPa)	α_{11}^{CNT} ($10^{-6}/\text{K}$)	α_{22}^{CNT} ($10^{-6}/\text{K}$)
300	5.6466	7.0800	1.9445	3.4584	5.1682
500	5.5308	6.9348	1.9643	4.5361	5.0189
700	5.4744	6.8641	1.9644	4.6677	4.8943

2014). Geometrical properties of the plate are $a = b = 200 \text{ mm}$ and $h = 20 \text{ mm}$. Specifications of the impactor are $E_i = 207 \text{ GPa}$, $\nu_i = 0.3$ and $\rho_i = 7960 \text{ kg/m}^3$, $R = 6.35 \text{ mm}$, and initial velocity $V_0 = 3 \text{ m/s}$. Material properties of the matrix and CNTs are shown in Tables 2, 3. Comparison is done in Fig. 4, when three types of distributions of the CNTs are set. In Ref. (Wang *et al.* 2014), material properties of FG-CNTRCs are estimated though the rule of mixture approach and the equations of motion are solved with the two step perturbation technique, whereas in the present paper, The Eshelby-Mori-Tanaka approach is employed to calculate those properties and the FEM is developed to solve the problem. However, as Fig. 4 reveals, there is a good agreement between present results and with the published results by (Wang *et al.* 2014).

4.2 Parametric studies

In this section, response of laminated functionally FG-CNTRC plate subjected to nonlinear low-velocity impact is investigated. A plate with dimensions of $0.200 \times 0.200 \times 0.02 \text{ (m)}$ and the

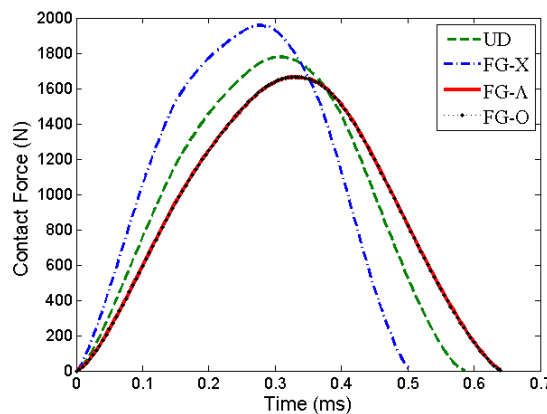


Fig. 5 Effect of graded profile of CNTs on the contact force history of fully clamped CNTRC laminate at room temperature ($V_{CN}^* = 0.28$)

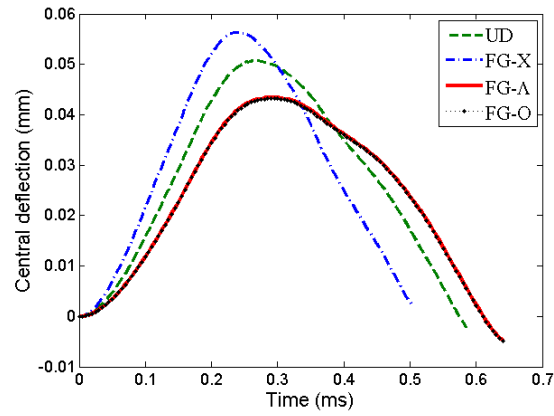


Fig. 6 Effect of graded profile of CNTs on the central deflection history of fully clamped CNTRC laminate at room temperature ($V_{CN}^* = 0.28$)

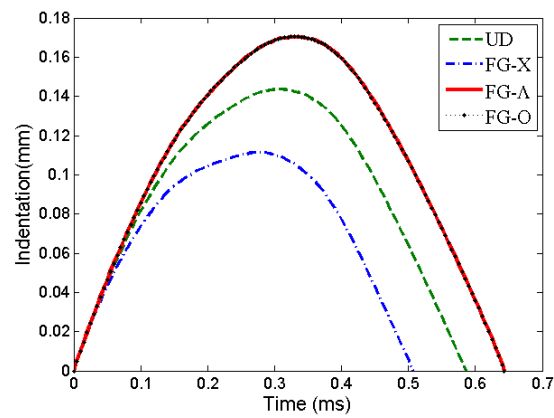


Fig. 7 Effect of graded profile of CNTs on the indentation value of fully clamped CNTRC laminate at room temperature ($V_{CN}^* = 0.28$)

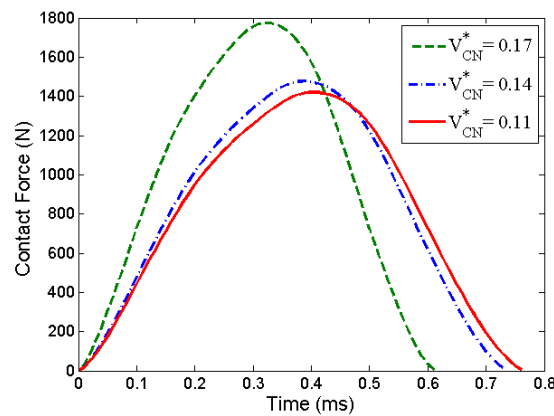


Fig. 8 Effect of volume fraction of CNTs on the contact force history of fully clamped FG-X CNTRC laminate at room temperature

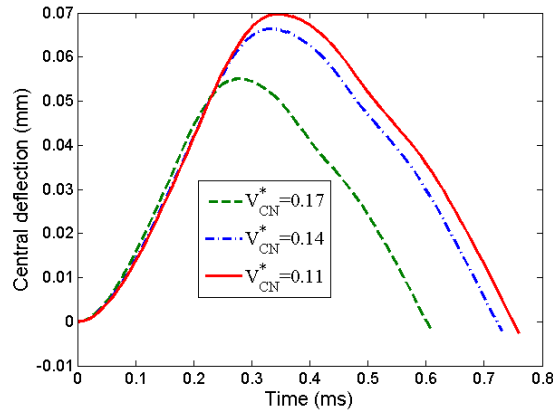


Fig. 9 Effect of volume fraction of CNTs on the central deflection history of fully clamped FG-X CNTRC laminate at room temperature

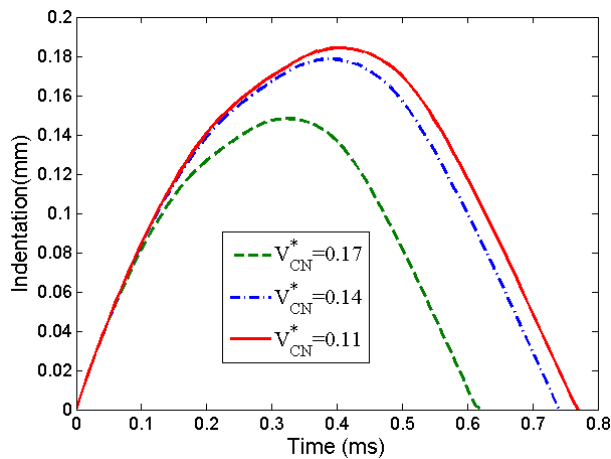


Fig. 10 Effect of volume fraction of CNTs on the indentation value of fully clamped FG-X CNTRC laminate at room temperature

stacking sequence [0/90/0/90/0] is considered. The Poly (methyl methacrylate), referred to as PMMA, is selected for the matrix. Table 2 represents the material properties of the composite matrix. The uniform temperature variation was applied to the plate, and the reference temperature is assumed to be $T_0 = 300$ (room temperature) in this study. Han and Elliott (2007) obtained relatively low values of modulus for (10, 10) SWCNTs ($E_{11}^{CNT} = 600 \text{ GPa}$, $E_{22}^{CNT} = 10 \text{ GPa}$, $G_{12}^{CNT} = 17.2 \text{ GPa}$) since the effective thickness of CNTs was assumed as 0.34 nm.

It is reported that the effective thickness of SWCNTs should be smaller than 0.142 nm and the effective wall thickness obtained for (10, 10) SWCNTs is 0.067 nm, which satisfies the Vodenitcharova–Zhang criterion (Wang and Zhang 2008). Thus the material properties reported by Zhang and Shen obtained by MD simulations are used for the present study (Shen and Zhang 2010), which is listed in Table 3. The impactor is made from steel with radius $R = 20.8 \text{ mm}$, and initial velocity $V_0 = 1 \text{ m/s}$, material properties of $E_i = 207 \text{ GPa}$, $\nu_i = 0.3$ and $\rho_i = 7960 \text{ kg/m}^3$.

4.2.1 Effect of graded profile of CNTs

In this section the effect of material property gradient on the contact force, indentation, and central deflection of the plate is analyzed. Four different grading profiles, namely, UD, FG-X, FG- Λ and FG-O are taken into account. Numerical results are depicted in Figs. 5-7, for different grading profiles and $V_{CN}^* = 0.28$. Plate at reference temperature is considered.

As may be observed, the laminated FG-CNT composite FG-CNTRC laminate of type X has shortest contact time duration and the most contact force while the laminate of type O and Λ have the least contact force and the most contact time among the four. Transverse Young's modulus of the surface is maximum for FG-X, followed by UD, FG-O and FG- Λ . Due to this reason, the laminate of type X has the least peak indentation and the most peak central deflection. On the other hand, the laminates of type O and Λ have the highest central deflection and the minimum indentation.

4.2.2 Effect of volume fraction of CNTs

Effect of volume fraction of CNTs on the contact force, indentation, central deflection of the

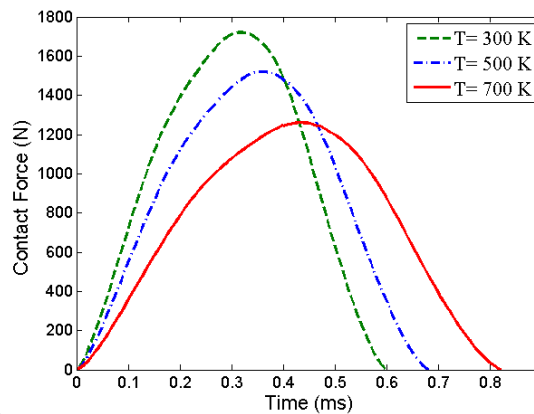


Fig. 11 Effect of temperature on the contact force history of fully clamped FG-X CNTRC laminate ($V_{CN}^* = 0.17$)

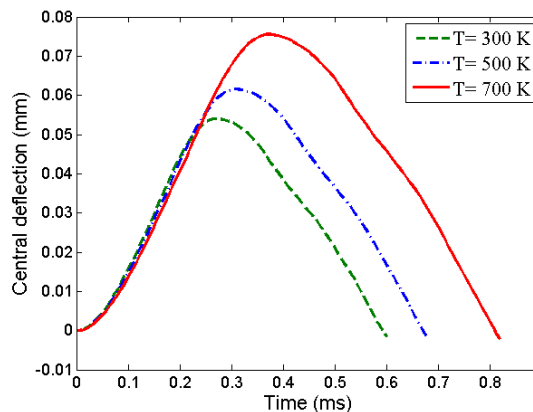


Fig. 12 Effect of temperature on the central deflection history of fully clamped FG-X CNTRC laminate ($V_{CN}^* = 0.17$)

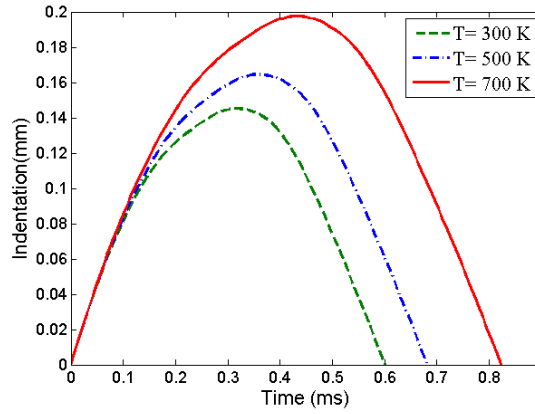


Fig. 13 Effect of temperature on the indentation value of fully clamped FG-X CNTRC laminate ($V_{CN}^* = 0.17$)

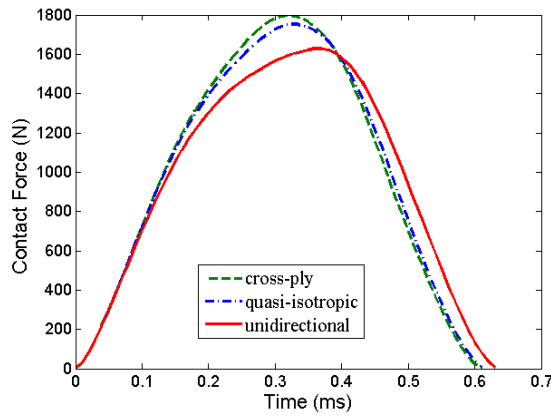


Fig. 14 Effect of stacking sequence on the contact force history of fully clamped FG-X CNTRC laminate at room temperature ($V_{CN}^* = 0.17$)

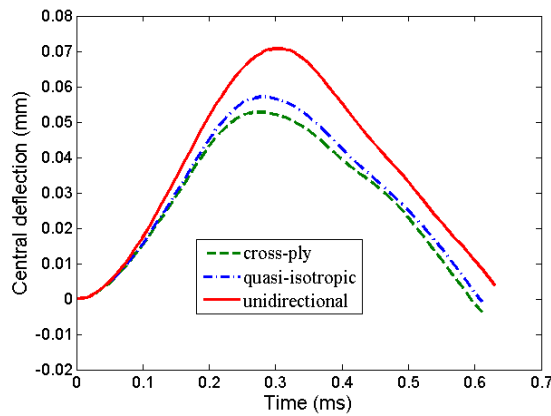


Fig. 15 Effect of stacking sequence on the central deflection history of fully clamped FG-X CNTRC laminate at room temperature ($V_{CN}^* = 0.17$)

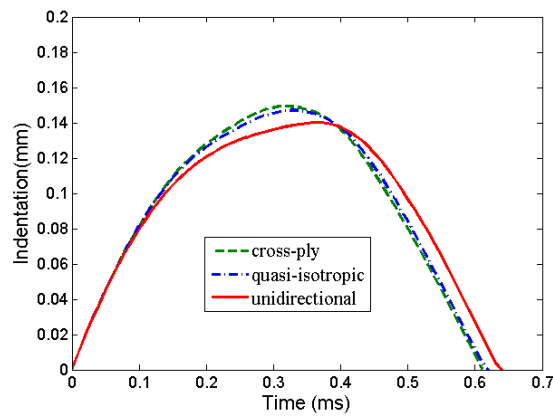


Fig. 16 Effect of stacking sequence on the indentation value of fully clamped FG-X CNTRC laminate at room temperature ($V_{CN}^* = 0.17$)

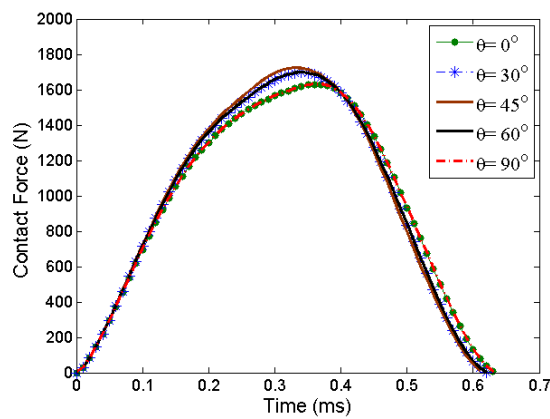


Fig. 17 Effect of lamination angle on the contact force history of fully clamped FG-X angle-ply $[-\theta / \theta / \theta / -\theta]$ CNTRC laminate at room temperature ($V_{CN}^* = 0.17$)

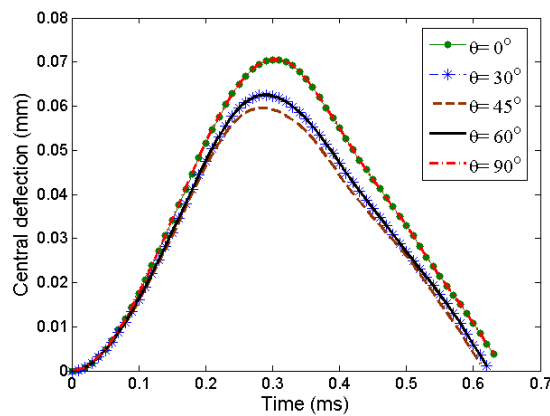


Fig. 18 Effect of lamination angle on the central deflection history of fully clamped FG-X angle-ply $[-\theta / \theta / \theta / -\theta]$ CNTRC laminate at room temperature ($V_{CN}^* = 0.17$)

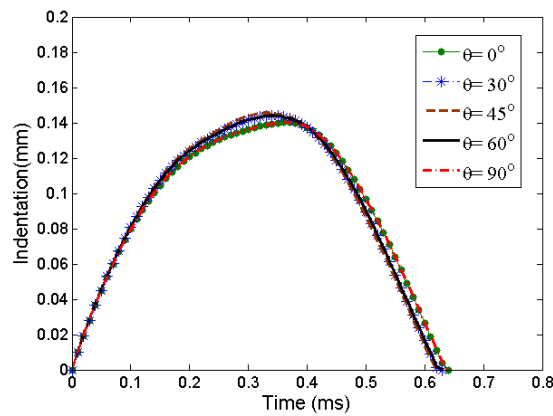


Fig. 19 Effect of lamination angle on the indentation value of fully clamped FG-X angle-ply $[-\theta / \theta / \theta / -\theta]$ CNTRC laminate at room temperature ($V_{CN}^* = 0.17$)

plate, and velocity of impactor is analyzed in this section. An FG-X CNT laminate with three different volume fraction of CNT, $V_{CN}^* = 0.11, 0.14$ and 0.17 are considered. Specifications are the same with the preceding section. Numerical results are depicted in Figs. 8-10. Since increasing the volume fraction index increases volume fraction of CNTs at the contact region, it leads to increased contact stiffness and the peaks of the time histories of the contact force and a decreased peak indentation. Increasing the volume fraction CNTs leads to a plate with higher bending rigidity. Therefore, the contact time duration and central deflection has decreased with increasing the volume fraction index. It should be noted that the difference between curves for the $V_{CN}^* = 0.17$ and $V_{CN}^* = 0.14$ is more than the difference between curves for the $V_{CN}^* = 0.14$ and $V_{CN}^* = 0.11$ mainly due to the difference between CNT efficiency parameters corresponding to the $V_{CN}^* = 0.17$ and $V_{CN}^* = 0.14$.

4.2.3 Effect of temperature changes in thermal environment

In this section, it is intended to investigate effect of temperature rise parameter on the impact response of a FG-CNTRC laminate. Three temperature parameters $T = 300, 500$ and 700 K are considered. For an FG-X CNT laminate with $V_{CN}^* = 0.17$ numerical results are depicted in Figs. 11-13. As may be observed, as the plate temperature increases contact time and central deflection increase while decreases the contact force. That is because increasing the plate temperature leads to structure loses stiffness generally. Also the effect of thermal condition on the indentation is same to the central deflection.

4.2.4 Effect of layup (Stacking Sequence)

In present section, to illustrate the dependency of the FG-CNT composite laminate to stacking sequence, four types of layup: Quasi Isotropic $[0/45/-45/90]_s$, Cross Ply $[0/90/0/90]_2$, Unidirectional 90 $[90]_8$, Unidirectional 0 $[0]_8$ are investigated. The number of layers is taken to 8. Plate is assumed at reference temperature. Specifications are the same with the preceding section. Time histories of the indentation, central deflection of the plate and contact force, are depicted in Figs. 17-19. As may be noted, the cross-ply composite plate has the least peak central deflection and the greatest contact force. On the other hand, the unidirectional composite plate has the highest central deflection and the minimum contact force.

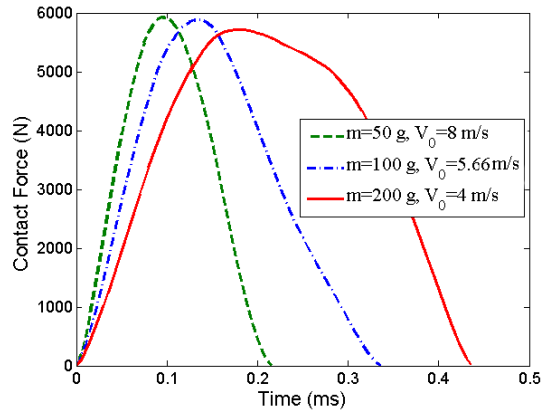


Fig. 20 Effect of mass and velocity of the impactor in a constant impact energy level on the contact force history of fully clamped FG-X CNTRC laminate at room temperature ($V_{CN}^* = 0.17$)

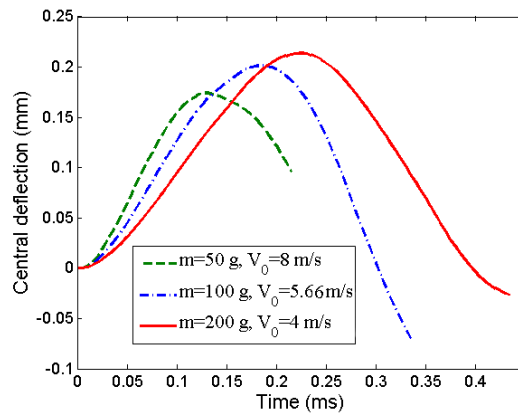


Fig. 21 Effect of mass and velocity of the impactor in a constant impact energy level on the central deflection history of fully clamped FG-X CNTRC laminate at room temperature ($V_{CN}^* = 0.17$)

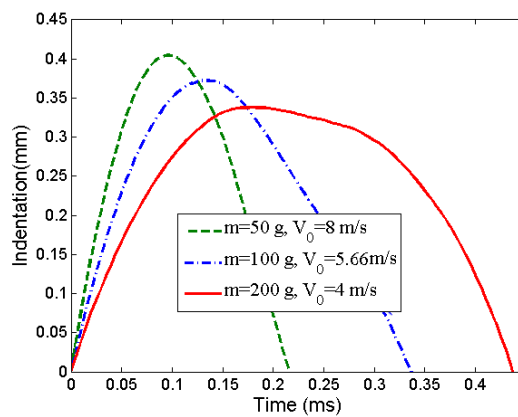


Fig. 22 Effect of mass and velocity of the impactor in a constant impact energy level on the indentation value of fully clamped FG-X CNTRC laminate at room temperature ($V_{CN}^* = 0.17$)

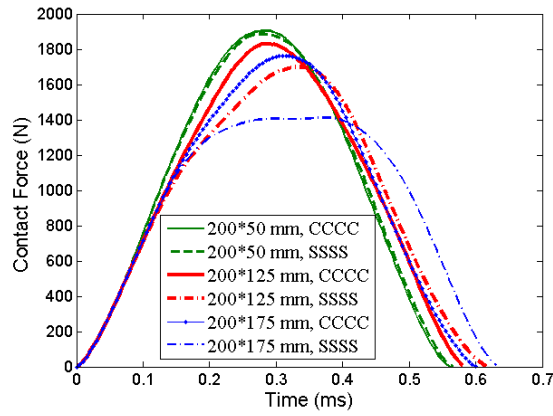


Fig. 23 Effect of in-plane dimensions under two boundary conditions on the contact force history of FG-X CNTRC laminate at room temperature ($V_{CN}^* = 0.17$)

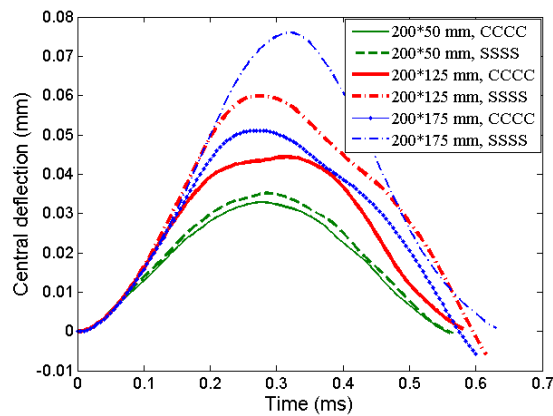


Fig. 24 Effect of in-plane dimensions under two boundary conditions on the central deflection history of FG-X CNTRC laminate at room temperature ($V_{CN}^* = 0.17$)

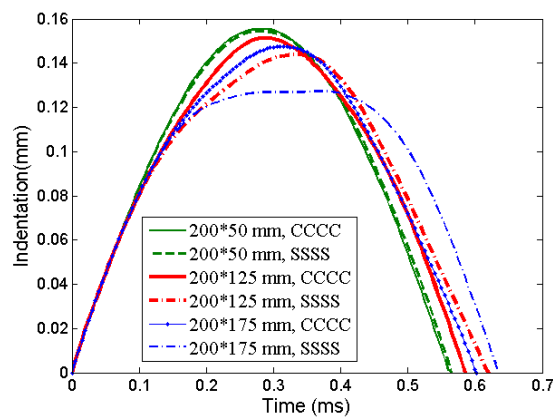


Fig. 25 Effect of in-plane dimensions under two boundary conditions on the indentation value of FG-X CNTRC laminate at room temperature ($V_{CN}^* = 0.17$)

The indentation value is maximum for unidirectional composite plate, followed by quasi-isotropic and cross-ply composites. In other configurations, influence of lamination angle for 4 layers angle-ply $[-\theta / \theta / \theta / -\theta]$ FG-CNT composite laminate is provided in Figs. 14-16. As seen from the results of this figures, the peaks contact force and indentation increase as the lamination angle θ changes from 0 to 45, and decrease when the lamination angle θ changes from 45 to 90. Besides, laminate plate with $\theta = 45$ has the minimum peak central deflection.

4.2.5 Effect of mass and velocity of the impactor in a constant energy level

In this section, parameters are the same with the preceding section, with exception of values of the mass and initial velocity of the impactor. In this regard, three combinations of the impactor mass and velocity are considered:

- (1) $m = 50$ g , $V = 8$ m/s
- (2) $m = 100$ g , $V = 5.66$ m/s
- (3) $m = 200$ g , $V = 4$ m/s

which all of this combinations result in an impact energy level equal to 1.6 J. results of this section are depicted Figs. 20-22. As may be noted from these figures, as the velocity increases (the impactor mass decreases with a lower rate), the peaks of central deflection decreases whereas indentation and contact force increases and the peak deflection and contact force are achieved in earlier time instants. Thus, the shocking effect of the impact force that transfers to the plate increases and a stronger impact is inflicted up on the nanocomposite.

4.2.6 Effect of in-plane dimensions under two boundary conditions

Effect of plate dimensions on response of laminated FG-CNTRC under nonlinear low-velocity impact under two boundary conditions is investigated in this section. Three sizes of $[0/90/0/90/0]$ FG-X CNT laminate ($V_{CN}^* = 0.17$) are considered: 200×174 mm², 200×125 mm², and 200×50 mm²

Table 4 Effect of in-plane dimensions under two boundary conditions on the peak contact force (KN) of CNTRC laminate at room temperature

V_{CN}^*		200×175 mm ²		200×125 mm ²		200×50 mm ²	
		CCCC	SSSS	CCCC	SSSS	CCCC	SSSS
0.11	UD	1.3661	1.1238	1.4063	1.3240	1.4665	1.4491
	FG-O	1.3288	1.1111	1.3557	1.2895	1.4167	1.4007
	FG-Λ	1.3294	1.1174	1.3578	1.2931	1.4169	1.4014
	FG-X	1.4095	1.1370	1.4649	1.3628	1.5244	1.5091
0.14	UD	1.4019	1.1952	1.4351	1.3712	1.4937	1.4785
	FG-O	1.3517	1.1751	1.3688	1.3238	2.1666	1.4154
	FG-Λ	1.3530	1.1808	1.3693	1.3268	1.4281	1.4161
	FG-X	1.4643	1.2167	1.5166	1.4273	1.5742	1.5607
0.17	UD	1.6668	1.3873	1.7041	1.6171	1.7784	1.7582
	FG-O	1.5929	1.3626	1.6086	1.5498	1.6789	1.6651
	FG-Λ	1.5944	1.3697	1.6091	1.5536	1.6791	1.6659
	FG-X	1.7612	1.4128	1.8307	1.6989	1.9049	1.8858

Table 5 Effect of in-plane dimensions under two boundary conditions on the peak central deflection (m) of CNTRC laminate at room temperature

V_{CN}^*	200×175 mm ²		200×125 mm ²		200×50 mm ²		
	CCCC	SSSS	CCCC	SSSS	CCCC	SSSS	
0.11	UD	6.2593×10 ⁻⁵	9.3435×10 ⁻⁵	5.5199×10 ⁻⁵	7.3231×10 ⁻⁵	4.0413×10 ⁻⁵	4.3394×10 ⁻⁵
	FG-O	6.0204×10 ⁻⁵	9.1325×10 ⁻⁵	5.3695×10 ⁻⁵	7.1009×10 ⁻⁵	3.8673×10 ⁻⁵	4.1756×10 ⁻⁵
	FG-Λ	5.9842×10 ⁻⁵	9.0443×10 ⁻⁵	5.3380×10 ⁻⁵	7.0225×10 ⁻⁵	3.8626×10 ⁻⁵	4.1620×10 ⁻⁵
	FG-X	6.4871×10 ⁻⁵	9.5324×10 ⁻⁵	5.6415×10 ⁻⁵	7.5401×10 ⁻⁵	4.1971×10 ⁻⁵	4.4802×10 ⁻⁵
0.14	UD	5.8885×10 ⁻⁵	8.5113×10 ⁻⁵	5.2844×10 ⁻⁵	6.6979×10 ⁻⁵	3.9162×10 ⁻⁵	4.1680×10 ⁻⁵
	FG-O	5.5748×10 ⁻⁵	8.1985×10 ⁻⁵	5.0786×10 ⁻⁵	6.3885×10 ⁻⁵	3.6879×10 ⁻⁵	3.9447×10 ⁻⁵
	FG-Λ	5.5442×10 ⁻⁵	8.1196×10 ⁻⁵	5.0634×10 ⁻⁵	6.3219×10 ⁻⁵	3.6843×10 ⁻⁵	3.9330×10 ⁻⁵
	FG-X	6.1824×10 ⁻⁵	8.7794×10 ⁻⁵	5.4419×10 ⁻⁵	7.0041×10 ⁻⁵	4.1163×10 ⁻⁵	4.3502×10 ⁻⁵
0.17	UD	4.8066×10 ⁻⁵	7.2947×10 ⁻⁵	4.2720×10 ⁻⁵	5.6674×10 ⁻⁵	3.0827×10 ⁻⁵	3.3260×10 ⁻⁵
	FG-O	4.4807×10 ⁻⁵	6.9410×10 ⁻⁵	4.0641×10 ⁻⁵	5.3342×10 ⁻⁵	2.8766×10 ⁻⁵	3.0943×10 ⁻⁵
	FG-Λ	4.4525×10 ⁻⁵	6.8698×10 ⁻⁵	4.0494×10 ⁻⁵	5.2716×10 ⁻⁵	2.8733×10 ⁻⁵	3.0831×10 ⁻⁵
	FG-X	5.1141×10 ⁻⁵	7.5965×10 ⁻⁵	4.4357×10 ⁻⁵	5.9917×10 ⁻⁵	3.2857×10 ⁻⁵	3.5122×10 ⁻⁵

under four edges fully clamped and four edges simply supported. Numerical results of this section are provided in Figs. 23-25. As the width of the plate decreases contact stiffness and the peaks of the time histories of the contact force increase and consequently peak indentation decreases. Besides, central deflection and contact time duration decreases permanently as the width of the plate decreases. The reason is that with decreasing the width of the plate, the supports of the plate become close to each other.

Table 6 Effect of in-plane dimensions under two boundary conditions on the indentation value (m) of FG-X CNTRC laminate at room temperature

V_{CN}^*	200×175 mm ²		200×125 mm ²		200×50 mm ²		
	CCCC	SSSS	CCCC	SSSS	CCCC	SSSS	
0.11	UD	1.9576×10 ⁻⁴	1.7188×10 ⁻⁴	1.9959×10 ⁻⁴	1.9173×10 ⁻⁴	2.0524×10 ⁻⁴	2.0362×10 ⁻⁴
	FG-O	2.0753×10 ⁻⁴	1.8420×10 ⁻⁴	2.1033×10 ⁻⁴	2.0342×10 ⁻⁴	2.1659×10 ⁻⁴	2.1496×10 ⁻⁴
	FG-Λ	2.0770×10 ⁻⁴	1.8490×10 ⁻⁴	2.1041×10 ⁻⁴	2.0380×10 ⁻⁴	2.1661×10 ⁻⁴	2.1503×10 ⁻⁴
	FG-X	1.8326×10 ⁻⁴	1.5881×10 ⁻⁴	1.8804×10 ⁻⁴	1.7919×10 ⁻⁴	1.9309×10 ⁻⁴	1.9180×10 ⁻⁴
0.14	UD	1.9378×10 ⁻⁴	1.7422×10 ⁻⁴	1.9681×10 ⁻⁴	1.9093×10 ⁻⁴	2.0214×10 ⁻⁴	2.0076×10 ⁻⁴
	FG-O	2.0888×10 ⁻⁴	1.9027×10 ⁻⁴	2.1064×10 ⁻⁴	2.0600×10 ⁻⁴	2.1666×10 ⁻⁴	2.1540×10 ⁻⁴
	FG-Λ	2.0902×10 ⁻⁴	1.9088×10 ⁻⁴	2.1069×10 ⁻⁴	2.0630×10 ⁻⁴	2.1668×10 ⁻⁴	2.1546×10 ⁻⁴
	FG-X	1.7747×10 ⁻⁴	1.5686×10 ⁻⁴	1.8168×10 ⁻⁴	1.7448×10 ⁻⁴	1.8625×10 ⁻⁴	1.8519×10 ⁻⁴
0.17	UD	1.6513×10 ⁻⁴	1.4611×10 ⁻⁴	1.6759×10 ⁻⁴	1.6183×10 ⁻⁴	1.7243×10 ⁻⁴	1.7112×10 ⁻⁴
	FG-O	1.8103×10 ⁻⁴	1.6313×10 ⁻⁴	1.8221×10 ⁻⁴	1.7775×10 ⁻⁴	1.8749×10 ⁻⁴	1.8646×10 ⁻⁴
	FG-Λ	1.8115×10 ⁻⁴	1.6370×10 ⁻⁴	1.8226×10 ⁻⁴	1.7804×10 ⁻⁴	1.8751×10 ⁻⁴	1.8652×10 ⁻⁴
	FG-X	1.4750×10 ⁻⁴	1.2735×10 ⁻⁴	1.5136×10 ⁻⁴	1.4400×10 ⁻⁴	1.5542×10 ⁻⁴	1.5438×10 ⁻⁴

Also, as can be observed, the FG-X CNT laminate with CCCC boundary condition had the higher peak contact force and indentation, and consequently lower central deflection. This is because the constraint of simply supported boundary condition is weaker than clamped boundary condition. It should be noted that, since decreasing the width of the plate increases contact stiffness, it leads to a decreased difference between curves for CCCC and SSSS boundary conditions, so that for the plate with the smallest in-plane dimensions ($200 \times 50 \text{ mm}^2$) no significant change in peaks of central deflection, contact force and indentation is observed when changes in the boundary conditions from SSSS to CCCC are made. In order to see better the effect of in-plane dimensions on the contact force, indentation, and central deflection of the plate for CCCC and SSSS boundary conditions, Tables 4-6 also illustrate this effect for of the different Distribution and volume fraction of CNTs.

5. Conclusions

Response of laminated FG-CNTRC plate under nonlinear low-velocity impact in thermal environments is studied using the finite element method. The four-noded rectangular conforming element with 15 DOF at each node based on HSDT and C^1 -continuity of the generalized displacement functions is employed. The Eshelby-Mori-Tanaka approach is employed to calculate the effective properties of materials of the laminated nanocomposite plates. Results are to evaluate the effects of varied parameters. It is concluded that:

- FG-CNTRC laminate of type X has the most contact force and shortest contact time duration while the laminate of type O and Λ have the least peak contact force and the most contact time among the four.
- Increasing the volume fraction of CNTs leads to an increased the contact force and consequently a decreased peak indentation. The contact time duration and central deflection has decreased with increasing the volume fraction index.
- Temperature is a significant factor in impact Behavior. As the plate temperature increases contact time and peak of central deflection and indentation increase while decreases the peak contact force.
- The cross-ply composite plate has the least peak central deflection and the greatest peak contact force. On the other hand, the unidirectional composite plate has the minimum peak contact force and the highest peak central deflection.
- In a constant impact energy level, as the velocity increases (the impactor mass decreases with a lower rate), the peaks of central deflection decreases whereas indentation and contact force increases and the peak deflection and contact force are achieved in earlier time instants. Thus, the shocking effect of the impact force that transfers to the plate increases and a stronger impact is inflicted up on the structure.
- As the width of the plate decreases the peak of contact force increase whereas contact time duration and peak of indentation and central deflection decrease.
- The FG-X CNT laminate with CCCC boundary condition had the higher peak contact force and indentation, and consequently lower central deflection. Decreasing the width of the plate leads to decreased difference between curves for CCCC and SSSS boundary conditions.

References

- Alibeigloo, A. and Liew, K. (2013), "Thermoelastic analysis of functionally graded carbon nanotube-reinforced composite plate using theory of elasticity", *Compos. Struct.*, **106**, 873-881.
- Aragh, B.S., Barati, A.N. and Hedayati, H. (2012), "Eshelby–Mori–Tanaka approach for vibrational behavior of continuously graded carbon nanotube-reinforced cylindrical panels", *Compos. Part B: Eng.*, **43**(4), 1943-1954.
- Arani, A.G., Maghamikia, S., Momammadimehr, M. and Arefmanesh, A. (2011), "Buckling analysis of laminated composite rectangular plates reinforced by SWCNTs using analytical and finite element methods", *J. Mech. Sci. Technol.*, **25**(3), 809-820.
- Benveniste, Y. (1987), "A new approach to the application of Mori-Tanaka's theory in composite materials", *Mech. Mater.*, **6**(2), 147-157.
- Delfosse, D., Vaziri, R., Pierson, M. and Poursartip, A. (1993), "Analysis of the non-penetrating impact behaviour of CFRP laminates", *ICCM/9. Composite Behaviour*, **5**, 366-373.
- Ebrahimi, F. and Habibi, S. (2016), "Deflection and vibration analysis of higher-order shear deformable compositionally graded porous plate", *Steel Compos. Struct., Int. J.*, **20**(1), 205-225.
- Ebrahimi, F. and Barati, M.R. (2016a), "Magneto-electro-elastic buckling analysis of nonlocal curved nanobeams", *Eur. Phys. J. Plus*, **131**(9), 346.
- Ebrahimi, F. and Barati, M.R. (2016b), "Static stability analysis of smart magneto-electro-elastic heterogeneous nanoplates embedded in an elastic medium based on a four-variable refined plate theory", *Smart Mater. Struct.*, **25**(10), 105014.
- Ebrahimi, F. and Barati, M.R. (2016c), "Temperature distribution effects on buckling behavior of smart heterogeneous nanosize plates based on nonlocal four-variable refined plate theory", *Int. J. Smart Nano Mater.*, **7**(3), 119-143.
- Ebrahimi, F. and Barati, M.R. (2016d), "An exact solution for buckling analysis of embedded piezo-electro-magnetically actuated nanoscale beams", *Adv. Nano Res., Int. J.*, **4**(2), 65-84.
- Ebrahimi, F. and Barati, M.R. (2016e), "Buckling analysis of smart size-dependent higher order magneto-electro-thermo-elastic functionally graded nanosize beams", *J. Mech.*, 1-11.
- Ebrahimi, F. and Barati, M.R. (2016f), "Buckling analysis of nonlocal third-order shear deformable functionally graded piezoelectric nanobeams embedded in elastic medium", *J. Brazil. Soc. Mech. Sci. Eng.*, 1-16.
- Ebrahimi, F. and Barati, M.R. (2016g), "Magnetic field effects on buckling behavior of smart size-dependent graded nanoscale beams", *Eur. Phys. J. Plus*, **131**(7), 1-14.
- Ebrahimi, F. and Barati, M.R. (2016h), "Vibration analysis of nonlocal beams made of functionally graded material in thermal environment", *Eur. Phys. J. Plus*, **131**(8), 279.
- Ebrahimi, F. and Barati, M.R. (2016i), "Vibration analysis of smart piezoelectrically actuated nanobeams subjected to magneto-electrical field in thermal environment", *J. Vib. Control*, 1077546316646239.
- Ebrahimi, F. and Barati, M.R. (2016j), "A nonlocal higher-order refined magneto-electro-viscoelastic beam model for dynamic analysis of smart nanostructures", *Int. J. Eng. Sci.*, **107**, 183-196.
- Ebrahimi, F. and Barati, M.R. (2016k), "Small-scale effects on hygro-thermo-mechanical vibration of temperature-dependent nonhomogeneous nanoscale beams", *Mech. Adv. Mater. Struct.*, 1-13.
- Ebrahimi, F. and Barati, M.R. (2016l), "A unified formulation for dynamic analysis of nonlocal heterogeneous nanobeams in hygro-thermal environment", *Applied Physics A*, **122**(9), 792.
- Ebrahimi, F. and Barati, M.R. (2016m), "Electromechanical buckling behavior of smart piezoelectrically actuated higher-order size-dependent graded nanoscale beams in thermal environment", *Int. J. Smart Nano Mater.*, **7**(2), 69-90.
- Ebrahimi, F. and Barati, M.R. (2016n), "Wave propagation analysis of quasi-3D FG nanobeams in thermal environment based on nonlocal strain gradient theory", *Appl. Phys. A*, **122**(9), 843.
- Ebrahimi, F. and Barati, M.R. (2016o), "Flexural wave propagation analysis of embedded S-FGM nanobeams under longitudinal magnetic field based on nonlocal strain gradient theory", *Arab. J. Sci. Eng.*, 1-12.

- Ebrahimi, F. and Barati, M.R. (2016p), "Buckling analysis of piezoelectrically actuated smart nanoscale plates subjected to magnetic field", *J. Intell. Mater. Syst. Struct.*, 1045389X16672569.
- Ebrahimi, F. and Barati, M.R. (2016q), Size-dependent thermal stability analysis of graded piezomagnetic nanoplates on elastic medium subjected to various thermal environments. *Applied Physics A*, **122**(10), 910.
- Ebrahimi, F. and Barati, M.R. (2016r), "Static stability analysis of smart magneto-electro-elastic heterogeneous nanoplates embedded in an elastic medium based on a four-variable refined plate theory", *Smart Mater. Struct.*, **25**(10), 105014.
- Eshelby, J.D. (1957), "The determination of the elastic field of an ellipsoidal inclusion, and related problems", *Proceedings of the Royal Society of London A: Mathematical, Physical and Engineering Sciences*. The Royal Society, pp. 376-396.
- Esawi, A.M. and Farag, M.M. (2007), "Carbon nanotube reinforced composites: potential and current challenges", *Mater. Design*, **28**(9), 2394-2401.
- Formica, G., Lacarbonara, W. and Alessi, R. (2010), "Vibrations of carbon nanotube-reinforced composites", *J. Sound Vib.*, **329** (10), 1875-1889.
- Han, Y. and Elliott, J. (2007), "Molecular dynamics simulations of the elastic properties of polymer/carbon nanotube composites", *Computat. Mater. Sci.*, **39**(2), 315-323.
- Heydarpour, Y., Aghdam, M. and Malekzadeh, P. (2014), "Free vibration analysis of rotating functionally graded carbon nanotube-reinforced composite truncated conical shells", *Compos. Struct.*, **117**, 187-200.
- Jam, J. and Kiani, Y. (2015), "Low velocity impact response of functionally graded carbon nanotube reinforced composite beams in thermal environment", *Compos. Struct.*, **132**, 35-43.
- Jooybar, N., Malekzadeh, P. and Fiouz, A. (2016), "Vibration of functionally graded carbon nanotubes reinforced composite truncated conical panels with elastically restrained against rotation edges in thermal environment", *Compos. Part B: Eng.*, **106**, 242-261.
- Kim, M., Park, Y.-B., Okoli, O.I. and Zhang, C. (2009), "Processing, characterization, and modeling of carbon nanotube-reinforced multiscale composites", *Compos. Sci. Technol.*, **69** (3), 335-342.
- Lei, Z., Liew, K.M. and Yu, J. (2013), "Buckling analysis of functionally graded carbon nanotube-reinforced composite plates using the element-free kp-Ritz method", *Compos. Struct.*, **98**, 160-168.
- Lei, Z., Zhang, L. and Liew, K. (2015), "Free vibration analysis of laminated FG-CNT reinforced composite rectangular plates using the kp-Ritz method", *Compos. Struct.*, **127**, 245-259.
- Li, X., Gao, H., Scrivens, W.A., Fei, D., Xu, X., Sutton, M.A., Reynolds, A.P. and Myrick, M.L. (2007), "Reinforcing mechanisms of single-walled carbon nanotube-reinforced polymer composites", *J. Nanosci. Nanotech.*, **7**(7), 2309-2317.
- Liew, K., Lei, Z. and Zhang, L. (2015), "Mechanical analysis of functionally graded carbon nanotube reinforced composites: A review", *Compos. Struct.*, **120**, 90-97.
- Malekzadeh, P. and Dehbozorgi, M. (2016), "Low velocity impact analysis of functionally graded carbon nanotubes reinforced composite skew plates", *Compos. Struct.*, **140**, 728-748.
- Malekzadeh, P. and Shojaee, M. (2013), "Buckling analysis of quadrilateral laminated plates with carbon nanotubes reinforced composite layers", *Thin-Wall. Struct.*, **71**, 108-118.
- Malekzadeh, P. and Zarei, A. (2014), "Free vibration of quadrilateral laminated plates with carbon nanotube reinforced composite layers", *Thin-Wall. Struct.*, **82**, 221-232.
- Mura, T. (2013), *Micromechanics of Defects in Solids*, Springer Science & Business Media.
- Qian, D., Dickey, E.C., Andrews, R. and Rantell, T. (2000), "Load transfer and deformation mechanisms in carbon nanotube-polystyrene composites", *Appl. Phys. Lett.*, **76**(20), 2868-2870.
- Rafiee, R. and Moghadam, R.M. (2012), "Simulation of impact and post-impact behavior of carbon nanotube reinforced polymer using multi-scale finite element modeling", *Computat. Mater. Sci.*, **63**, 261-268.
- Rafiee, M., Liu, X., He, X. and Kitipornchai, S. (2014), "Geometrically nonlinear free vibration of shear deformable piezoelectric carbon nanotube/fiber/polymer multiscale laminated composite plates", *J. Sound Vib.*, **333**(14), 3236-3251.
- Reddy, J.N. (2004), *Mechanics of Laminated Composite Plates and Shells: Theory and Analysis*, CRC press.
- Sahoo, N.G., Rana, S., Cho, J.W., Li, L. and Chan, S.H. (2010), "Polymer nanocomposites based on

- functionalized carbon nanotubes”, *Progress Polym. Sci.*, **35**(7), 837-867.
- Seidel, G.D. and Lagoudas, D.C. (2006), “Micromechanical analysis of the effective elastic properties of carbon nanotube reinforced composites”, *Mech. Mater.*, **38**(8), 884-907.
- Shen, H.-S. (2009), “Nonlinear bending of functionally graded carbon nanotube-reinforced composite plates in thermal environments”, *Compos. Struct.*, **91**(1), 9-19.
- Shen, H.-S. (2011), “Postbuckling of nanotube-reinforced composite cylindrical shells in thermal environments, Part I: Axially-loaded shells”, *Compos. Struct.*, **93**(8), 2096-2108.
- Shen, H.-S. and Zhang, C.-L. (2010), “Thermal buckling and postbuckling behavior of functionally graded carbon nanotube-reinforced composite plates”, *Mater. Des.*, **31**(7), 3403-3411.
- Shen, H.-S. and Zhang, C.-L. (2012a), “Non-linear analysis of functionally graded fiber reinforced composite laminated plates, Part I: Theory and solutions”, *Int. J. Non-Linear Mech.*, **47**(9), 1045-1054.
- Shen, H.-S. and Zhang, C.-L. (2012b), “Non-linear analysis of functionally graded fiber reinforced composite laminated plates, Part II: Numerical results”, *Int. J. Non-Linear Mech.*, **47**(9), 1055-1064.
- Shenas, A.G., Malekzadeh, P. and Ziaee, S. (2017), “Vibration analysis of pre-twisted functionally graded carbon nanotube reinforced composite beams in thermal environment”, *Compos. Struct.*, **162**, 325-340.
- Shu, X. and Sun, L. (1994), “Thermomechanical buckling of laminated composite plates with higher-order transverse shear deformation”, *Comput. Struct.*, **53**(1), 1-7.
- Spitalsky, Z., Ttasis D., Papagelis, K. and Galiotis, C. (2010), “Carbon nanotube–polymer composites: chemistry, processing, mechanical and electrical properties”, *Progress Polym. Sci.*, **35**(3), 357-401.
- Sun, C. and Chen, J. (1985), “On the impact of initially stressed composite laminates”, *J. Compos. Mater.*, **19**(6), 490-504.
- Vaziri, R., Quan, X. and Olson, M. (1996), “Impact analysis of laminated composite plates and shells by super finite elements”, *Int. J. Impact Eng.*, **18**(7), 765-782.
- Wang, J. and Pyrz, R. (2004), “Prediction of the overall moduli of layered silicate-reinforced nanocomposites—part I: basic theory and formulas”, *Compos. Sci. Technol.*, **64**(7), 925-934.
- Wang, Z.-X. and Shen, H.-S. (2011), “Nonlinear vibration of nanotube-reinforced composite plates in thermal environments”, *Computat. Mater. Sci.*, **50**(8), 2319-2330.
- Wang, Z.-X. and Shen, H.-S. (2012a), “Nonlinear dynamic response of nanotube-reinforced composite plates resting on elastic foundations in thermal environments”, *Nonlinear Dyn.*, **70**(1), 735-754.
- Wang, Z.-X. and Shen, H.-S. (2012b), “Nonlinear vibration and bending of sandwich plates with nanotube-reinforced composite face sheets”, *Compos. Part B: Eng.*, **43**(2), 411-421.
- Wang, C. and Zhang, L. (2008), “A critical assessment of the elastic properties and effective wall thickness of single-walled carbon nanotubes”, *Nanotechnology*, **19**(7), 075705.
- Wang, Z.-X., Xu, J. and Qiao, P. (2014), “Nonlinear low-velocity impact analysis of temperature-dependent nanotube-reinforced composite plates”, *Compos. Struct.*, **108**, 423-434.
- Yang, S. and Sun, C. (1982), “Indentation law for composite laminates”, *Proceedings of the 6th Conference on Composite Materials: Testing and Design*, ASTM International.
- Yas, M. and Heshmati, M. (2012), “Dynamic analysis of functionally graded nanocomposite beams reinforced by randomly oriented carbon nanotube under the action of moving load”, *Appl. Math. Model.*, **36**(4), 1371-1394.
- Zhang, L., Lei, Z., Liew, K. and Yu, J. (2014), “Large deflection geometrically nonlinear analysis of carbon nanotube-reinforced functionally graded cylindrical panels”, *Comput. Method. Appl. Mech. Eng.*, **273**, 1-18.
- Zhu, P., Lei, Z. and Liew, K.M. (2012), “Static and free vibration analyses of carbon nanotube-reinforced composite plates using finite element method with first order shear deformation plate theory”, *Compos. Struct.*, **94**(4), 1450-1460.
- Zienkiewicz, O.C. and Taylor, R.L. (2005), *The Finite Element Method for Solid and Structural Mechanics*, Butterworth-heinemann.